The Astrophysical Journal, 937:59 (13pp), 2022 October 1 https://doi.org/10.3847/1538-4357/ac88cb

Magnetic Helicity Evolution and Eruptive Activity in NOAA Active Region 11158

L. M. Green[1], J. K. Thalmann[2], G. Valori[3], E. Pariat[4], L. Linan[5], and K. Moraitis[6]
[1] Mullard Space Science Laboratory, UCL, Holmbury St. Mary, Dorking, Surrey, RH5 6NT, UK; lucie.green@ucl.ac.uk
[2] University of Graz, Institute of Physics/IGAM, Graz, Austria
[3] Max-Planck-Institut für Sonnensystemforschung, Göttingen, Germany
[4] Sorbonne Université, École polytechnique, Institut Polytechnique de Paris, Université Paris-Saclay, Observatoire de Paris, CNRS, Laboratoire de Physique des Plasmas (LPP), Paris, France
[5] Centre for Mathematical Plasma Astrophysics, KU Leuven, Leuven, Belgium
[6] Physics Department, University of Ioannina, Ioannina 45110, Greece
Received 2022 January 1; revised 2022 August 5; accepted 2022 August 9; published 2022 September 28

Abstract

Coronal mass ejections are among the Sun's most energetic activity events yet the physical mechanisms that lead to their occurrence are not yet fully understood. They can drive major space weather impacts at Earth, so knowing why and when these ejections will occur is required for accurate space weather forecasts. In this study we use a 4 day time series of a quantity known as the helicity ratio, $|H_J|/|H_V|$ (helicity of the current-carrying part of the active region field to the total relative magnetic helicity within the volume), which has been computed from nonlinear force-free field extrapolations of NOAA active region 11158. We compare the evolution of $|H_J|/|H_V|$ with the activity produced in the corona of the active region and show this ratio can be used to indicate when the active region is prone to eruption. This occurs when $|H_J|/|H_V|$ exceeds a value of 0.1, as suggested by previous studies. We find the helicity ratio variations to be more pronounced during times of strong flux emergence, collision and reconnection between fields of different bipoles, shearing motions, and reconfiguration of the corona through failed and successful eruptions. When flux emergence, collision, and shearing motions have lessened, the changes in helicity ratio are somewhat subtle despite the occurrence of significant eruptive activity during this time.

Unified Astronomy Thesaurus concepts: Solar activity (1475); Solar active regions (1974); Solar magnetic fields (1503); Solar coronal mass ejections (310); Space weather (2037)

1. Introduction

One of the most striking forms of activity that takes place in the evolving magnetic field of the solar corona is a coronal mass ejection (CME). These eruptions derive their energy from the coronal magnetic field (Forbes 2000) and send $\sim 10^{12}$ kg of magnetized plasma into the heliosphere where they can have a significant space weather impact (see Chen 2011 and Temmer 2021 for a reviews of observations and space weather impacts of CMEs). The rapid expansion of the magnetic field structure at the onset of a CME is likely due to an ideal MHD instability (Kliem & Török 2006), loss of equilibrium (Forbes & Isenberg 1991; van Ballegooijen & Mackay 2007), or runaway magnetic reconnection (Antiochos et al. 1999; Moore et al. 2001). Once the CME is underway, there is a close dynamical coupling between ideal and nonideal processes (Toriumi & Wang 2019). However, in order to fully understand a CME's occurrence, processes that are at play in the hours, days, or weeks before the CME onset must also be studied, as it is during this time that the energy that powers a CME is accumulated, in the form of field-aligned electric currents, and the magnetic field evolves into its eruptive state (for a review, see, e.g., Shibata & Magara 2011). Processes such as sunspot rotation, flux cancellation or reconnection in the corona can act as mechanisms to bring the coronal field to a state in which an ideal instability/loss of equilibrium or runaway reconnection occurs to drive the CME into the heliosphere (see Green et al. 2018 for a review of mechanisms). However, it is not yet clear whether certain mechanisms dominate, whether certain combinations are required, or whether a specific magnetic field configuration, e.g., a flux rope, needs to be built by these mechanisms. This leads to the criteria for which an ideal instability, loss of equilibrium, or runaway magnetic reconnection occur being poorly understood.

A quantity that has shown promise in advancing our knowledge of which CME processes are the key ones is magnetic helicity (e.g., Green et al. 2002; Démoulin 2007; Dalmasse et al. 2013; Yeates & Hornig 2016; Patsourakos & Georgoulis 2017). Magnetic helicity is a signed scalar quantity that measures the 3D complexity of a magnetic field within a volume, and its cascade to larger size scales could help build eruptive structures. The application of magnetic helicity to the coronal magnetic field uses a form known as relative magnetic helicity, H_V (Berger & Field 1984), which can be decomposed into two components (Berger 2003). First, H_J, which represents the helicity associated with the current-carrying part of the magnetic field and, second, H_{PJ}, which is the helicity associated with the volume-threading field. The information provided by the current-carrying field component has been used in a helicity ratio, $|H_J|/|H_V|$ (see Section 1.1 for details), which has shown promise in determining the likelihood of a CME and other activity events such as coronal jets (Pariat et al. 2017; Linan et al. 2018; see Section 1.2 for more detail). Some studies suggest that the helicity ratio increases in magnitude in the run-up to an eruption, and that an eruption only occurs once a threshold value has been reached (Moraitis et al. 2019; Thalmann et al. 2019b; Gupta et al. 2021; see Section 1.3 for more detail).

In this way, the helicity ratio shows the potential to reveal which physical mechanisms are the key ones operating in the

time leading up to a CME (when the helicity ratio is increasing) while making no assumptions about the specific magnetic field configuration of the CME source region (e.g., flux rope configuration versus sheared arcade). Instead, analysis of the helicity ratio will enable the development of an understanding of how the corona evolves in a more general way. The helicity ratio also shows potential for providing an eruption forecast relevant for space weather purposes with a longer lead time than is currently possible. For example, the UK's National Grid has stated a desire to have a 5 days advance warning of CME arrival and geomagnetic storm onset (Krausmann et al. 2016). Since CME travel time can be between ~1 and 4 days, there is a clear need for an eruption warning in advance of the event itself.

It should be noted, though, that implicit in the use of the helicity ratio as a way to determine which active regions are prone to an eruption is an assumption that any CME originates in the part of the magnetic field in which the electric currents are the strongest, because the helicity ratio increases in magnitude as the current-carrying portion of the field makes a more significant contribution to the volume-integrated ratio value. It is yet to be tested whether the helicity ratio as an indicator of potential eruptivity may be more suited to active regions that produce CMEs from the region's core, where the most highly sheared fields are normally located (Schmieder et al. 1996), as opposed to active regions that produce eruptions from their periphery. In addition, the method requires considering a volume that is sufficiently large in order to capture the eruptive structure that, for events such as stealth CMEs, may involve a structure at relatively high altitude (perhaps $>0.5\ R_\odot$ from the photosphere; O'Kane et al. 2019). The suitability of the helicity ratio to determine the eruptive potential of active regions across a wide range of characteristics is still to be assessed.

1.1. The Helicity Ratio

As already introduced, the eruptive potential of an active region can be quantified using the helicity ratio, $|H_J|/|H_V|$, where

$$H_V \equiv \int_{\mathcal{V}} (\boldsymbol{A} + \boldsymbol{A}_\mathrm{p}) \cdot (\boldsymbol{B} - \boldsymbol{B}_\mathrm{p})\, \mathrm{dV} \tag{1}$$

is the gauge-invariant relative magnetic helicity (referred to from here on just as magnetic helicity), given $\nabla \cdot \boldsymbol{B} = \nabla \cdot \boldsymbol{B}_\mathrm{p} = 0$ and $\hat{\boldsymbol{n}} \cdot \boldsymbol{B}_\mathrm{p} = \hat{\boldsymbol{n}} \cdot \boldsymbol{B}$ on the volume-bounding surface, $\partial\mathcal{V}$ (Berger & Field 1984; Finn & Antonsen 1985). Here, $\boldsymbol{B}$ represents the 3D vector magnetic field within the finite volume, $\mathcal{V}$, under study and $\boldsymbol{B}_\mathrm{p}$ is a chosen reference field, the two being linked to their respective vector potentials via $\boldsymbol{B} = \nabla \times \boldsymbol{A}$ and $\boldsymbol{B}_\mathrm{p} = \nabla \times \boldsymbol{A}_\mathrm{p}$. Furthermore,

$$H_J \equiv \int_{\mathcal{V}} (\boldsymbol{A} - \boldsymbol{A}_\mathrm{p}) \cdot (\boldsymbol{B} - \boldsymbol{B}_\mathrm{p})\, \mathrm{dV}, \tag{2}$$

linked to H_V in Equation (1) via $H_V = H_J + H_{PJ}$ (Berger 1999), where

$$H_{PJ} \equiv 2 \int_{\mathcal{V}} \boldsymbol{A}_\mathrm{p} \cdot (\boldsymbol{B} - \boldsymbol{B}_\mathrm{p})\, \mathrm{dV}. \tag{3}$$

While H_J in Equation (2) represents the helicity associated with the current-carrying magnetic field, $\boldsymbol{B}_J = \boldsymbol{B} - \boldsymbol{B}_\mathrm{p}$ (therefore also called the "nonpotential helicity"), H_{PJ} is the helicity of the volume-threading field (therefore also called the "potential" helicity). Despite being independently gauge invariant, H_J and H_{PJ} are not conserved in ideal MHD due to the existence of a gauge-invariant term that enables the exchange between them, unlike H_V, which has the property of being well conserved (Linan et al. 2018). Therefore, H_V is uniquely bound to the topological properties (structure) of the magnetic field, in contrast to dissipative quantities like magnetic energy.

1.2. Pioneering Simulation-based Work

The increased attention being paid to the study of $|H_J|/|H_V|$ originates from a few simulation-based works (e.g., Pariat et al. 2017; Zuccarello et al. 2018; Linan et al. 2018) that have suggested that $|H_J|/|H_V|$ successfully characterizes the eruptive potential of solar-like configurations which produce an eruption. Zuccarello et al. (2018) performed an analysis of parametric 3D MHD simulations that were carried out by Zuccarello et al. (2015), starting from the same nonpotential configuration, i.e., that of a sheared arcade formed due to footpoint shearing motions applied to an initially potential field. The individual simulation runs differed in the way in which solar-like motions on the photospheric boundary were defined, which led to the subsequent formation of an eruptive flux rope. A control case with only numerical diffusion as a controlling force was also performed, which did not produce any eruption. For the four eruptive simulations, numerous relaxation runs were performed in order to precisely determine the instant at which each configuration becomes unstable. Computing different magnetic energy and helicity quantities did not reveal a characteristic pre-eruption threshold. However, the situation is different for the ratio $|H_J|/|H_V|$: the magnetic system becomes eruptive for the same value of $|H_J|/|H_V|$ (within measurement precision), i.e displays a clear threshold behavior. It is worth noting that in the simulations of Zuccarello et al. (2015), the driver of the eruptive activity is believed to be the torus instability. That is, the eruptive activity occurred when the magnetic pressure in the current-carrying flux rope could no longer be balanced by the magnetic tension of the magnetic field overlying it. This raises the interesting question of whether there may be a relationship between the helicity ratio and the torus instability.

Linan et al. (2020), further analyzed the four eruptive simulations of Zuccarello et al. (2018). In particular, they studied the precise dynamics of the magnetic helicities, H_J and H_{PJ}. They found that while these simulations displayed similarities, the temporal evolution of helicity was very different from one simulation to the other. While in each simulation $|H_J|/|H_V|$ was monotonously increasing until reaching the threshold value when the eruption occurs, the precise dynamics of the evolution of H_J and H_{PJ} are sensitively different from one simulation to another. Linan et al. (2020) thus showed that the $|H_J|/|H_V|$ threshold for eruption can be reached in different ways with different helicity-related evolution, hence the details of the pre-eruptive evolution do not influence the helicity-related eruption onset threshold.

In the simulation of Zuccarello et al. (2018) the magnetic field configuration is created from an initially potential field in which nonpotentiality is introduced by boundary motions. However, on the Sun active regions form due to flux emergence (Green et al. 2018), implying that nonpotential fields are directly transferred from the solar interior. Active regions may be deterministically eruptive because of the

structure of the emerging field. Pariat et al. (2017) thus studied a series of parametric flux-emergence simulations leading to either eruptive or noneruptive solar-like active regions, that is, with a configuration in which a CME-like magnetic structure is ejected and one in which a flare-like reconfiguration occurred in a confined manner. It was observed that, unlike dissipative quantities such as magnetic flux and energy, helicity clearly discriminates between unstable (eruptive) and stable (noneruptive) numerical simulations. More interestingly, $|H_J|/|H_V|$ appeared to successfully characterize the eruptive potential of the simulations. $|H_J|/|H_V|$ indeed displayed significantly larger values for the system that eventually erupted compared to the noneruptive ones, and only before the eruption. Once the eruption occurred in the eruptive simulations, the values of $|H_J|/|H_V|$ became similar to the noneruptive simulations.

Other studies found a tight relation between $|H_J|/|H_V|$ and eruptive processes. The flux emergence simulations analyzed in Moraitis et al. (2014) displayed a strong correspondence between enhanced values of H_J and the generation of eruptions: the eruptive simulations exhibited significantly larger values of H_J prior to the CME-like ejection. Computing $|H_J|/|H_V|$, high values were obtained prior to the eruption onset, while the noneruptive flux emergence simulation displayed low and constant values (K. Moraitis, private communication). Here, again, $|H_J|/|H_V|$ seems to successfully characterize the eruptivity of the system. Finally, Linan et al. (2018), performed a corresponding analysis of numerical simulations of the formation of a coronal jet. In that work, the initial model setup consists of a 3D null point subject to twisting motions that result in helicity accumulation. Subsequent magnetic reconnection between the closed and open magnetic field associated with the null point induces the formation of a jet, followed by a slow relaxation toward the initial potential state. Importantly, the jet is triggered at a time when $|H_J|/|H_V|$ exhibits its highest values. Linan et al. (2018) emphasized the importance of corresponding observation-based applications, allowing these successful concepts to be applied to real solar cases.

1.3. Pioneering Observation-based Work

For observation-based studies of the coronal magnetic field, the relevant vector fields $\boldsymbol{B}$ and $\boldsymbol{B}_{\rm p}$ are typically estimated using nonlinear force-free (NLFF) and potential-field models, respectively, using the measured photospheric vector magnetic field as the lower boundary condition (for reviews see, e.g., Wiegelmann & Sakurai 2012 and Wiegelmann et al. 2017). Using $\boldsymbol{B}$ and $\boldsymbol{B}_{\rm p}$ as inputs (with the latter satisfying $\boldsymbol{B}_{\rm p} = \nabla\varphi$ and $(\hat{\boldsymbol{n}} \cdot \nabla\varphi)|=(\vec{\hat{n}} \cdot \boldsymbol{B})|$ on $\partial\mathcal{V}$) allows the computation of $\boldsymbol{A}$ and $\boldsymbol{A}_{\rm p}$ with high accuracy in Cartesian geometry using a so-called "finite-volume" (FV) method (for a review see Valori et al. 2016). Then, H_V, H_J, and H_{PJ} represent physically meaningful quantities that can be used to characterize the magnetic system within $\mathcal{V}$ and its time evolution if a series of models are used.

It should be noted that reliable estimates of helicity, as determined from observation-based models, can only be expected if the extrapolated magnetic field is solenoidal to a sufficient degree, i.e., if $\nabla \cdot \boldsymbol{B} = 0$ is sufficiently satisfied. The corresponding level of tolerance in such solar applications has been analyzed in depth, with an unpredictable effect on any subsequent FV helicity computation shown when suggested thresholds are exceeded (Thalmann et al. 2019a). Subsequently, Thalmann et al. (2020) were able to explicitly relate the degree of solenoidality to the reliability of the associated free magnetic energy estimates, finding that nonsolenoidality makes only a minimal contribution. The pioneering observation-based works that are summarized in the following discussion ensured and demonstrated a sufficient solenoidal quality of the input fields used for the helicity analysis.

James et al. (2018) used a magnetofrictional method to approximate the NLFF corona, in and around NOAA active region 11504 on 2012 June 14, in order to provide the first observation-based estimation of $|H_J|/|H_V|$, and found a value of $|H_J|/|H_V| = 0.17$ an hour before a CME-associated GOES M1.9 class flare. Subsequent single active region studies have dealt with the eruptivity of NOAA active region 12673 on 2017 September 6. Based on an optimization approach to approximate the corresponding coronal magnetic field, Moraitis et al. (2019) found values of $|H_J|/|H_V| \simeq 0.17$ prior to the occurrence of an eruptive X9.3 flare in NOAA active region 12673. This can be compared to the value of $|H_J|/|H_V| \approx 0.15$ determined from a time-dependent, data-driven simulation of the same event (Price et al. 2019). Another active region study using an optimization-based NLFF model of NOAA active region 11158 found values of $\gtrsim$0.17 prior to an eruptive X2.2 flare (Thalmann et al. 2019b). The consistent findings of these studies suggest that high values of $|H_J|/|H_V|$ are indeed indicating the potential of active regions to produce eruptive events. On the contrary, very low values of $|H_J|/|H_V|$ were found prior to confined (CME-less) GOES X-class flares that originated from NOAA active region 12192 ($|H_J|/|H_V| \lesssim 0.05$; Thalmann et al. 2019b). This led to the question of whether or not values of $|H_J|/|H_V|$ can be deduced for active regions and used to evaluate their eruptive potential. Indeed, in the multievent study most recently carried out by Gupta et al. (2021) it was found that values of $|H_J|/|H_V| \gtrsim 0.1$ characterize the model corona in the hours prior to CME occurrence, and that $|H_J|/|H_V|$ is distinctly lower in the coronal field of active regions prior to confined (CME-less) flares. This suggests that the pre-CME values of $|H_J|/|H_V|$ in active regions found by James et al. (2018), Moraitis et al. (2019), Price et al. (2019), and Thalmann et al. (2019b) may represent extreme cases.

1.4. This Study

The analysis presented here is based on the comparative work of Thalmann et al. (2019b), who analyzed the time evolution of the coronal helicity budget of NOAA active region 11158 over a ∼4 day period. A magnetogram cadence of 1 hr was used, except during times of intense flaring when the cadence was changed to 12 minutes. In Thalmann et al. (2019b), a NLFF (and corresponding potential field) model time series was used as the input to different FV helicity computation methods to retrieve the corresponding vector potentials, and to estimate the time evolution of $|H_J|/|H_V|$. The results revealed a close correspondence of the coronal helicity budgets deduced from the application of different FV methods; see Section 2.3.2 of Thalmann et al. (2019b) for details of the methods used to compute the helicity ratio time series. In our analysis, we use the mean of the helicity ratio values, as computed from the four time series of helicity ratios in Thalmann et al. (2019b), and the standard deviation of the data set provides an uncertainty that reflects the application of using different helicity methods. It was noted by Thalmann et al.

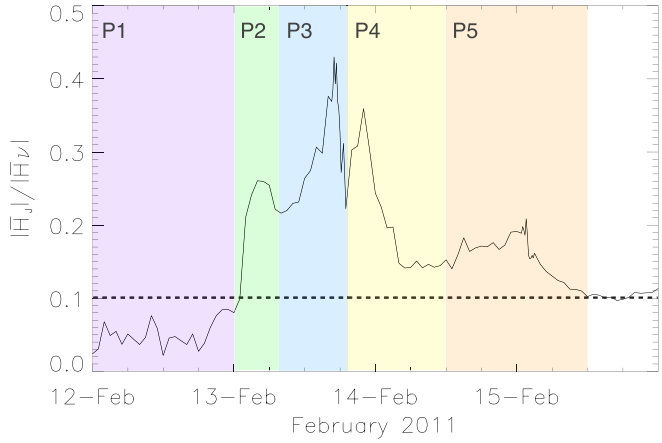

Figure 1. Evolution of the mean helicity ratio (continuous line) for the time period 2011 February 12–15, inclusive, and helicity ratio phases labeled P1 through P5 corresponding to Phase 1 through Phase 5 (colored panels). The threshold helicity ratio value of 0.1 is marked with a horizontal dashed line.

(2019b) that the temporal evolution of $|H_J|/|H_V|$ seems to respond to, e.g., strong flux emergence and the occurrence of CMEs (see their Figure 3(c)). A key aspect in the interpretation of the helicity ratio remained unexplored, though, namely, its response to coronal activity of differing magnitudes and types. This motivated us to analyze in more detail the time evolution of $|H_J|/|H_V|$ in relation to the observed overall evolution of the coronal magnetic field, on smaller spatial and temporal scales.

2. Helicity Ratio Evolution

The evolution of the helicity ratio and observed coronal activity of NOAA active region 11158 are analyzed in this study in five different phases (Figure 1). The selection of each phase is based on the observed evolution of the unsigned flux, free energy (E_f), and helicity ratio in NOAA active region 11158 in the time period 12 February 00:00 UT to 15 February 23:59 UT. Phase 1 shows a time period in which the helicity ratio remains below the "threshold" value, i.e., below 0.1, as proposed by Thalmann et al. (2019b) and Gupta et al. (2021), and when the coronal field is close to potential as determined from $\frac{E_f}{E} = 0.05$ (see Figure 3(a) of Thalmann et al. 2019b, i.e., little free magnetic energy content). Phase 2 covers the time period in which the helicity ratio shows a rapid rise, a peak, and the first time in which the threshold is exceeded. Phase 2 also covers the time during which there is a significant increase in unsigned flux in the active region (Figure 2(a): Thalmann et al. 2019b; Gupta et al. 2021; Figure 4(a), Sun et al. 2012), and electric current (Figure 4(b), Sun et al. 2012). Phase 3 marks the time period in which the helicity ratio starts to rise again and includes the time of the first major eruptive event from the region. Phase 4, again, covers a rapid rise of the helicity ratio, culminating in a major peak. Following Phase 4, there is a period during which the helicity ratio shows only minor variation, and Phase 5 starts just before a rapid increase of the helicity ratio value occurs and the time period includes the time of the eruptive X-class flare in the region. Phase 5 ends when the value of the helicity ratio drops to the threshold level of 0.1.

3. Results: Active Region Evolution

NOAA active region 11158 began to emerge in the southern hemisphere very late on 2011 February 9. Successive emergence and rapid motion of several bipoles was observed (e.g., Chintzoglou & Zhang 2013). The overall evolution of the photospheric magnetic field exhibited shearing motions, sunspot rotation, collision of opposite polarities, and flux cancellation, producing a complex active region with a high level of flaring and eruptive activity (e.g., Jiang et al. 2012; Sun et al. 2012; Vemareddy et al. 2012). A significant increase in electric currents and free magnetic energy occurred during the time period 14:30 UT February 12 to 04:30 UT February 13, with flux emergence injecting $\sim 10^{32}$ erg of free magnetic energy into the corona during those 10 hr (Sun et al. 2012; Thalmann et al. 2019b). The continued flux emergence led to a distinctive phase in the active region's evolution during February 13, when opposite polarities of two different emerging bipoles collided. Results from Chintzoglou et al. (2019) show these opposite polarities (named N1 and P2 in their notation) collided and exhibited their highest shearing motions on this day, with flux cancellation involving these two polarities commencing. The photospheric line-of-sight magnetic field evolution can be seen in Figure 2.

In the following sections we describe the evolution of the active region, from the photosphere to the corona, for the time period 2011 February 12–15, inclusive. To complete the observational analysis a wide range of data were used. The photospheric magnetic field evolution is analyzed using the Solar Dynamics Observatory (SDO)/Helioseismic and Magnetic Imager (HMI) line-of-sight magnetic field data (Scherrer et al. 2012), following the active region throughout the full duration of this study. Data from the SDO/Atmospheric Imaging Assembly (AIA; Lemen et al. 2012) are used to determine occurrences of energy deposition in the lower atmosphere using 1600 Å (upper photosphere) and 1700 Å (temperature minimum region) data. Eruptions and reconfigurations of the coronal field are determined through the analysis of the evolving plasma emission structures observed in the AIA 94 Å (imaging 6 MK plasma) and 193 Å (imaging 1.3 MK and 20 MK plasma) wavebands, and Hinode XRT data (Ti poly filter, imaging plasma at ∼10 MK; Golub et al. 2007). AIA 131 Å data are used to create an active region light curve for comparison with GOES X-Ray Sensor (XRS) 1–8 Å data for identification of active region flaring. During February 2011, STEREO-A and B were 87° and 94° from the Sun–Earth line, respectively. Solar TErrestrial RElations Observatory (STEREO) Extreme Ultraviolet Imager (EUVI) 195 Å (imaging 1.6 MK plasma) and inner coronagraph (COR1) data (Howard et al. 2008) were used for the analysis of the evolution of coronal emission structures and identification of CMEs from NOAA active region 11158.

3.1. Phase 1: 12 February 00:00 to 23:59 UT

The photospheric magnetic field distribution at the start of Phase 1 is composed of two bipoles that have emerged adjacent to each other ("Bipole 1" and "Bipole 2" in Figure 2). Both bipoles have positive polarity field in their leading spots but are inclined at different angles with respect to the east–west direction. During Phase 1, these two bipoles exhibit further emergence and separation of their polarities. By ∼18:00 UT on February 12 it is clear that a third bipole (Bipole 3) is emerging within Bipole 1. The emergence of Bipole 3 represents the major change to the photospheric field during Phase 1, and the negative flux of Bipole 3 appears to be spatially adjacent to that of Bipole 1. During this phase the photospheric field remains

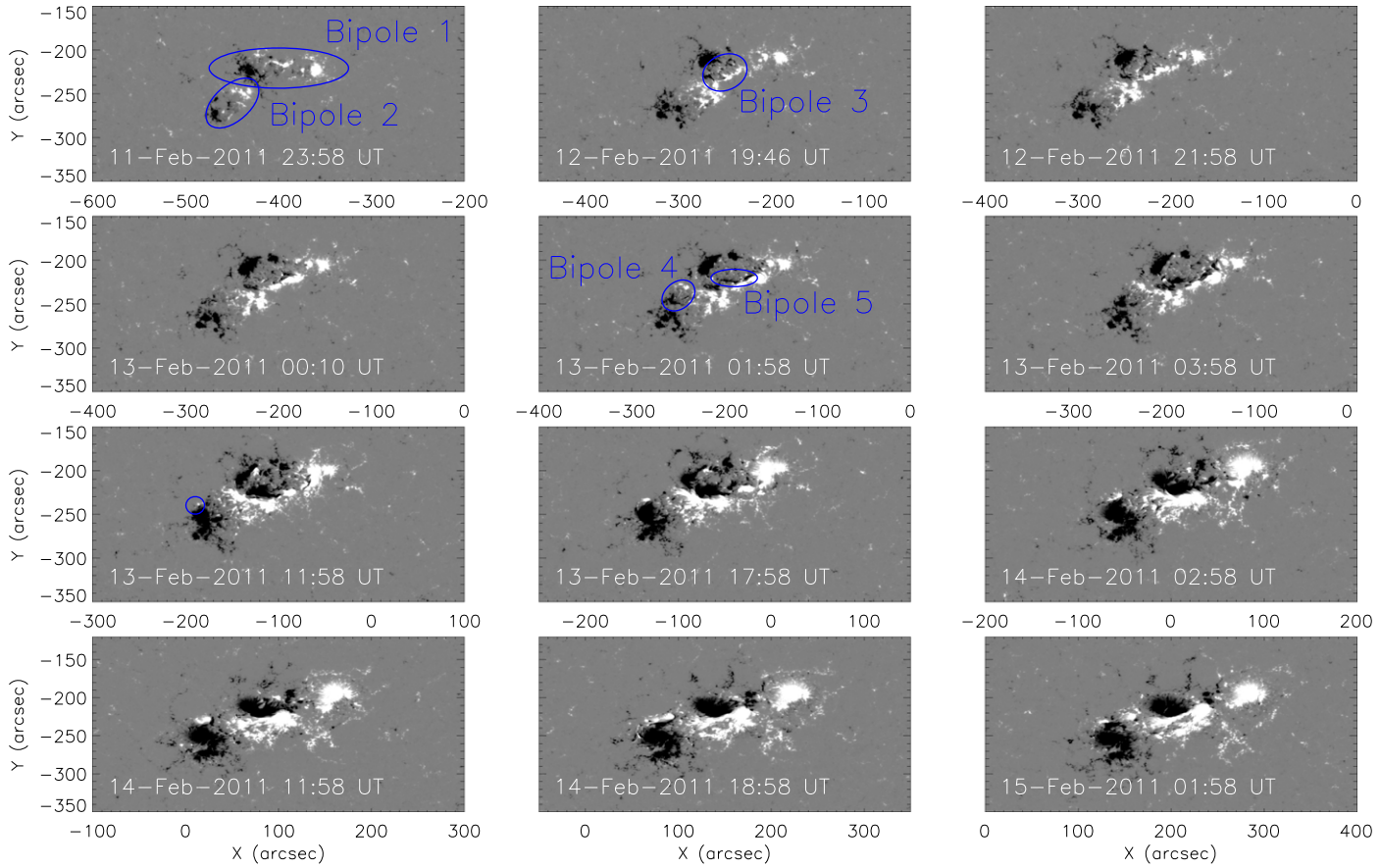

Figure 2. Evolution of the line-of-sight photospheric magnetic field as observed with SDO/HMI throughout all five phases. Bipoles that emerge during the time periods under study are indicated by blue ovals and discussed in the relevant sections.

fairly fragmented with only small spots observed in the white light HMI data.

GOES XRS data analyzed in concert with the AIA 131 Å light curve show that, although a series of B-class flares and one C-class flare occur during this phase, none originate in NOAA active region 11158. However, the 1600 Å waveband reveals brightenings associated with the serpentine nature of the emerging flux of Bipole 3, indicating the occurrence of small-scale magnetic reconnection taking place in the lower solar atmosphere.

During Phase 1, the helicity ratio oscillates around a value of 0.06 and remains below 0.1 at all times (although the value increases to close to 0.1 on February 12 ~20:00 UT; Figure 3). During this phase there is no major activity and no eruptive activity. The very small increase in the helicity ratio observed from ∼18:00 UT on February 12 is cotemporal with the emergence of Bipole 3.

3.2. Phase 2: February 13 00:00 to 07:00 UT

During Phase 2, the photospheric magnetic field continues to evolve with a new bipole (Bipole 4) emerging adjacent to Bipole 2 (Figure 2). The orientation of Bipole 4 matches that of Bipole 2 and the positive and negative polarity fragments of the two bipoles begin to merge. By the end of Phase 2, a fifth bipole (Bipole 5) has begun to emerge within Bipole 3. It is during this phase that the collision of opposite polarities in the center of the active region begins increasing the field gradient across the polarity inversion line between the positive polarity field of Bipole 2 and negative polarity field of Bipole 3.

AIA 1600 Å data show continued brightenings in the serpentine field associated with the emerging flux and, although GOES XRS data show small B-class flaring, only one B-class flare appears to originate in 11158. AIA 94 Å data show the growth of a new loop system by 00:25 UT on February 13 on the northern edge of the active region. This faint loop structure grows again ∼01:20 UT on February 13 and appears to start to erupt ∼02:10 UT on February 13. Post-eruption loops form as, and after, the erupting structure lifts off; these loops seem to have a second phase of growth ∼05:35 UT on February 13. This evolution of the corona is more clearly seen in soft X-ray data. Hinode X-Ray Telescope (XRT) images show apparent changes beginning ∼00:25 UT on February 13, when larger loops illuminate on the region's northern edge, leading to an expansion of the active region in this location (Figure 4). These loops begin to expand ∼01:40 UT in the northeast direction in the plane-of-the-sky and erupt in the same direction ∼02:40 UT. A soft X-ray cusp forms under the erupting structure, visible by ∼03:55 UT. This loop system seems to be connected to the positive polarity of Bipole 1 and the negative polarity of Bipole 3. These "cusp" loops undergo a second phase of expansion from ∼05:30 UT February 13 (note that there is an XRT data gap between 04:53 and 05:25 UT on February 13). However, the lack of any white light CME in STEREO-B COR1 data imply that no successful eruption occurred. Observations are therefore interpreted as showing a failed eruption ∼02:10 UT on February 13, as evidenced by the rising structure and formation of the cusp, with a further episode of reconnection in the coronal field ∼05:30 UT February 13.

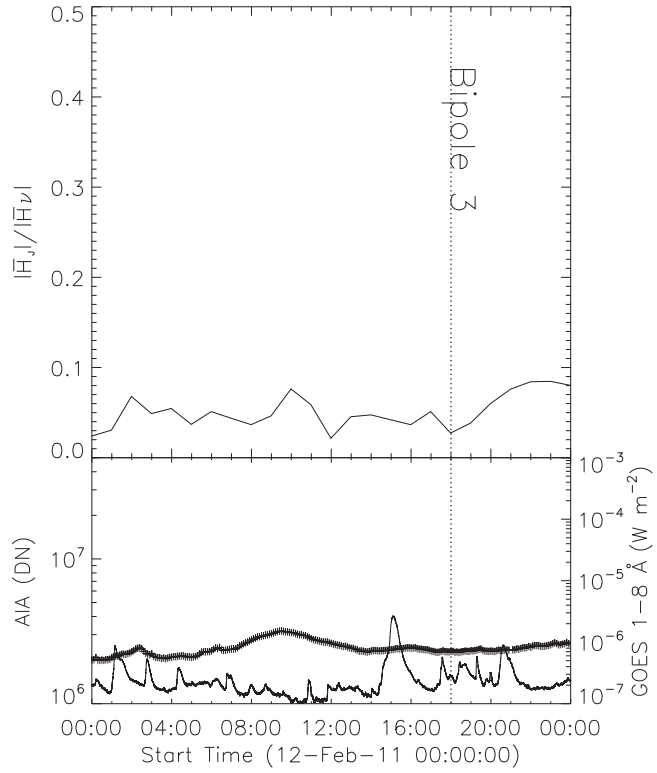

Figure 3. Evolution of the mean helicity ratio during Phase 1 (February 12 00:00 to 23:59 UT) is shown in the top panel (continuous line). The bottom panel shows the full Sun GOES light curve (continuous line) and the AIA 131 Å active region light curve. The vertical dotted black line indicates the start of the emergence of Bipole 3.

Approximately one hour before the failed eruption, the helicity ratio value exceeds 0.1. The $|H_J|/|H_V|$ ratio then shows a rounded peak ∼02:00 with a reduction in the ratio value ∼06:00 UT on February 13 (Figure 5).

3.3. Phase 3: February 13 07:00 to 19:00 UT

During Phase 3 there is a significant evolution of the photospheric magnetic field, including the continued emergence of flux and separation of polarities in Bipoles 4 and 5, counterclockwise rotation of the negative polarity of Bipole 5, and coalescence of the positive polarities of Bipole 1 and Bipole 3 (Figure 2). Collision of the negative flux of Bipole 5 and positive flux of Bipole 2 and Bipole 4 further builds the polarity inversion line in the center of the active region, along which strong shearing motions occur during this phase. In addition, there is the emergence of a small bipole on the northern edge of the negative polarity of Bipole 4 (indicated in a panel of Figure 2 at February 13 2011 11:58 UT). In response, the corona exhibits a range of activity during this phase.

The evolution of the corona during Phase 3 can be summarized as involving two main episodes of activity. The *first* episode of activity begins with a set of extreme-UV (EUV)-emitting loops that are observed to be rising in STEREO-A and STEREO-B EUVI data by 12:40 UT on 2011 February 13, accompanied by a C1.1 class flare beginning ∼12:29 UT. The location and altitude of these loops as seen from the STEREO-B perspective is indicated by the circle in the lower-left panel of Figure 6. Another C-class flare, which produced flare ribbons as seen in AIA 1700 Å data, is observed to begin ∼13:20 UT on February 13, indicating another episode of reconnection in the corona. A flare of GOES class C4.7 then occurs at ∼13:44 UT, cotemporal with a rising loop structure observed in XRT ∼13:30 UT, twin dimmings in AIA 94 Å running difference data, and flare ribbons around 13:50 UT on February 13 observed in AIA 1700 Å. The emission structure further rises ∼14:15 UT and becomes too faint to detect by ∼16:30 UT; meanwhile, what appear to be (post-eruption) flare loops grow underneath (Figure 6, XRT panel at 14:14 UT and EUVI panel at 14:13 UT). However, no clear white light CME counterpart is observed in association with the rising structure/flare ribbons/coronal dimming, so this event is assumed to be a failed eruption. The *second* episode of activity involves a GOES M6.6-class flare, global EUV wave, and a white light CME. Prominent AIA 1700 Å flare ribbons are observed by ∼17:33 UT on February 13, which are produced in association with the white light CME, which is first seen in STEREO-A COR1 data at 17:45 UT 2011 February 13. This episode of eruptive activity is well documented in previous analyses (e.g., Toriumi et al. 2013; Luoni et al. 2017).

During Phase 3, the helicity ratio remains at levels >0.25 at all times and rises to reach a peak value of >0.45 around 17:00 UT February 13 (Figure 7). The failed eruption appears to have only a minor impact on the helicity ratio, but there is a notable decrease in the helicity ratio after the M6.6 flare and CME. In summary, Phase 3 begins with a period of confined activity in which reconnection is reconfiguring the corona and ends with a successful eruption with an associated major flare.

3.4. Phase 4: February 13 19:00 to February 14 12:00 UT

During Phase 4, the line-of-sight photospheric magnetic field exhibits continued counterclockwise rotation of the negative polarity of Bipole 5 and westward motion of the positive polarities of Bipole 2 and Bipole 4, shearing them against the negative flux of Bipole 5 and creating a polarity inversion line that is approximately aligned in the east–west direction (Figure 2).

The corona is observed to be very dynamic during this phase, with the occurrence of significant jet activity observed in two time periods beginning February 13 21:25 UT and 23:00 UT. The latter time includes jets that occur contemporaneously on both the northern and southern sides of the active region. These jets are followed in time by a small white light CME first observed in STEREO-A COR1 by 02:55 UT on February 14. The onset time of this eruption in the lower corona is ∼02:30 UT February 14 as determined from a GOES C1.6-class flare and EUV wave that propagates northward from the active region, following the trajectory of many of the jets. A soft X-ray cusp observed in the wake of the CME completes the observational support that a successful eruption occurred. A second CME occurs during this phase, beginning in the lower corona ∼06:54 UT on February 14, as evidenced by a white light CME observed in STEREO-B COR1 by 07:10 UT on February 14 and (post-eruption) flare loops in the active region.

During Phase 4, the helicity ratio remains at levels >0.25, increasing to reach a peak value of 0.4 around 22:00 UT February 13 (Figure 8). The peak of the helicity ratio value corresponds in time with the jet activity observed in the active region, while the CME occurs while the ratio value is declining.

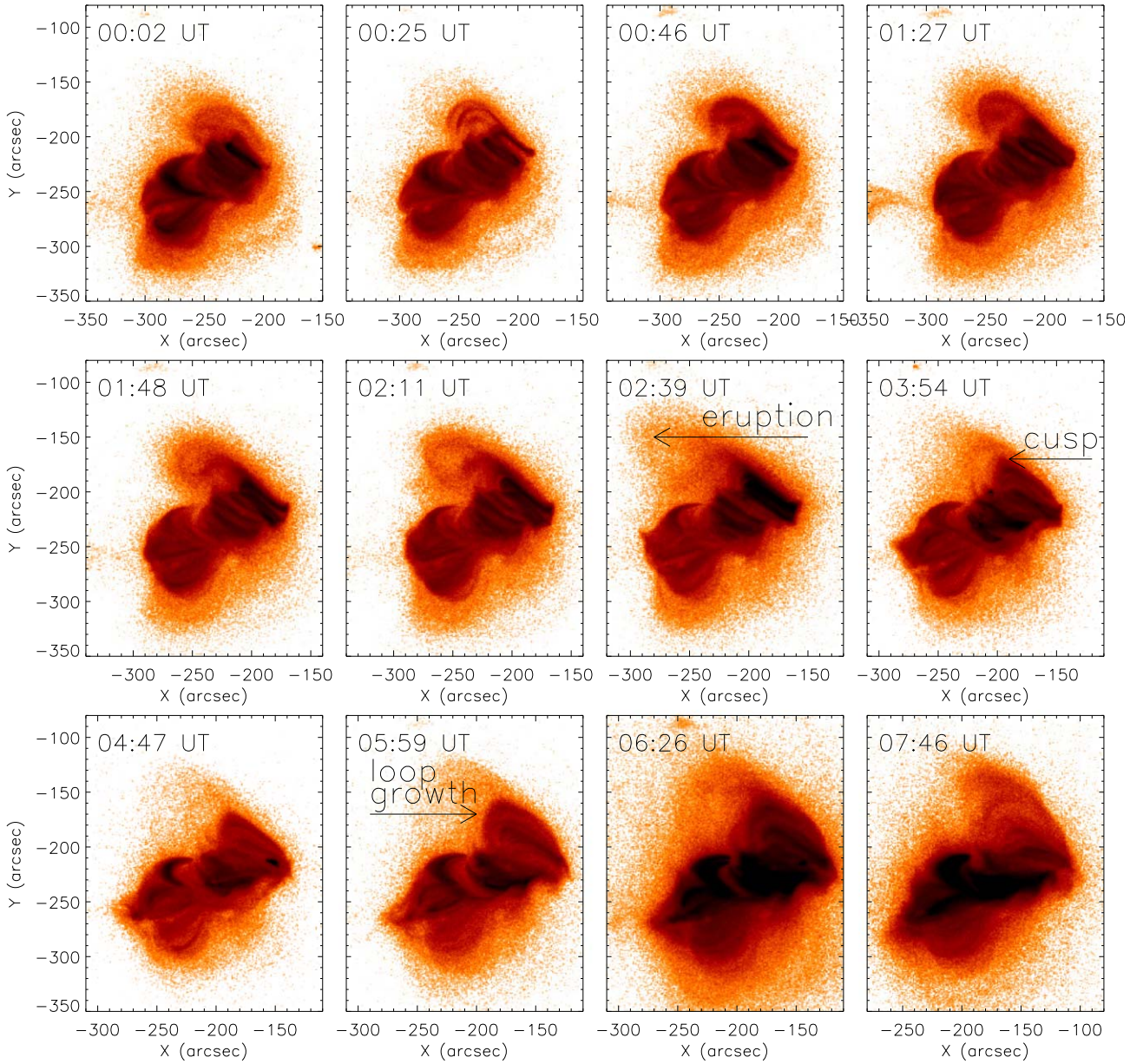

Figure 4. Phase 2: Hinode/XRT images on 2011 February 13 taken with the Ti poly filter. Data are displayed using a log scale to bring out fainter plasma emission structures. The images in the panels of the middle row show faint changes in the corona associated with a failed eruption, and in the bottom row a second phase of loop growth is shown.

3.5. Phase 5: February 14 12:00 to February 15 12:00 UT

The line-of-sight photospheric magnetic field evolution in Phase 5 shows further evolution of the polarity inversion line between the positive polarities of Bipole 2 and Bipole 4 against the negative flux of Bipole 5 (Figure 2). These positive polarities merge and move rapidly northwest, effectively causing the positive field to move in a counterclockwise direction around the negative polarity flux of Bipole 5. At the same time, the positive polarity fragment created by this merger rotated in a clockwise sense throughout Phase 5, as detailed in Jiang et al. (2012). The negative polarities of Bipole 5 and Bipole 1 also merge. The overall effect is to change the orientation of the main polarity inversion line from an east–west direction to a northwest, southeast orientation.

The corona continues to be dynamic, and the activity includes four CMEs. The first CME during this phase is observed in STEREO-A COR1 data on February 14 by 13:05 UT, with a CME onset determined from an EUV wave and a GOES C9.4-class flare on February 14 ∼12:40 UT. The second CME of this phase was seen in STEREO-A COR1 by February 14 17:35 UT. AIA data indicate eruption onset ∼17:20 UT, through the occurrence of an EUV wave that propagates predominantly to the north and a GOES M6.6-class flare. The third CME of this phase was observed in STEREO-A COR1 on February 14 by 19:55 UT with AIA data indicating eruption onset ∼19:25 UT. The fourth and final CME of this phase was associated with the GOES X2.2-class flare with an onset time ∼01:45 UT on 15 February. In addition to the successful eruptions, the active region produced jets on February 14 at ∼15:00 UT and on 15 February at ∼00:30 UT, 03:15 UT, 04:30 UT, 08:00 UT, and ∼09:00 UT. The latter two episodes of jet activity were smaller in spatial extent than those preceding.

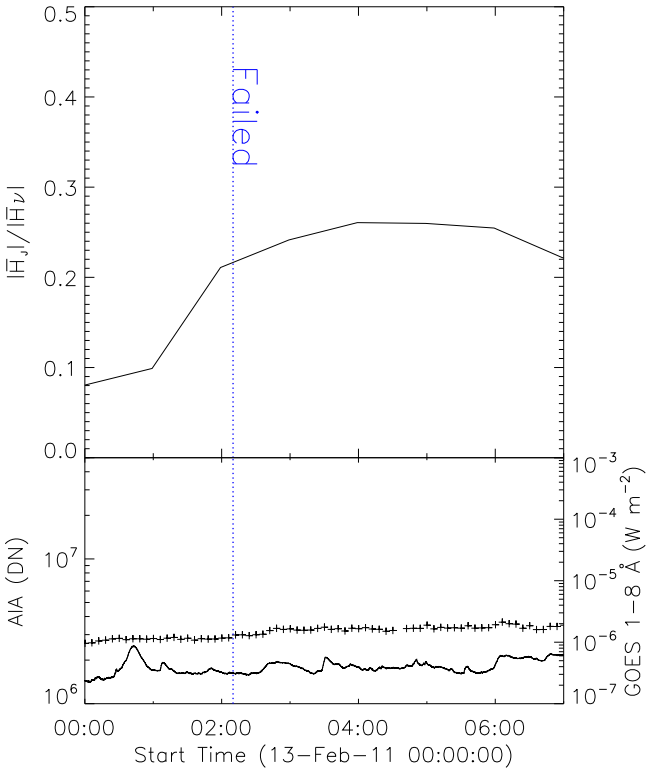

Figure 5. Evolution of the mean helicity ratio during Phase 2 (February 13 00:00 to 07:00 UT) shown in the top panel (continuous line). The bottom panel shows the full Sun GOES 1–8 Å light curve (continuous line) and the AIA 131 Å active region light curve. The vertical dotted blue line indicates the time of a failed eruption.

During Phase 5, the helicity ratio remains above 0.1 at all times and increases from 0.14 at the start of the phase to a peak value of 0.22 prior to the GOES X2.2-class flare (Figure 9). After Phase 5, the helicity ratio drops below the 0.1 threshold value and only just exceeds the threshold at the end of 15 February. After Phase 5 eruptive activity ceases, with the next CME not occurring until ∼14:20 UT on 2011 February 16. Additionally, the active region's increasing distance from central meridian make a reliable extrapolation and helicity computation more challenging after Phase 5.

4. Discussion

In this study we aim to probe how the helicity ratio evolves with respect to observed changes in the coronal magnetic field configuration. The helicity ratio used is the average value found from four time series of helicity ratios computed by the application of different FV helicity methods to a time series of NLFF models (see Thalmann et al. 2019b, for more details on the helicity ratio computation). In particular, we investigate changes in the helicity ratio related to the occurrence of CMEs. We find that the helicity ratio is a quantity that appears to be sensitive to the evolution of the coronal magnetic field, in line with findings of previous studies but with some variation. For example, during the times of major eruptive activity (i.e., the GOES X-class flare and associated CME on 2011 February 15) there are only small variations in the helicity ratio, although the ratio remains above the threshold value of 0.1. Here we discuss the evolution of the helicity ratio phase by phase.

During Phase 1 (12 February 00:00 to 23:59 UT), despite the emergence of new flux toward the end of the phase, the helicity ratio remains stable and below the proposed threshold for eruption for the entire time. This low value of the helicity ratio agrees with the observational evidence that no large-scale nonpotential coronal magnetic field structure has yet formed and that no eruptive activity is observed during this phase. The helicity ratio oscillates around a value of 0.06 but increases to values close to 0.1 after 20:00 UT on 12 February following the emergence of new flux into the active region that is observed to start ∼18:00 UT on 12 February. This only small increase of the helicity ratio at the end of Phase 1 is likely a consequence of there being no significant increase in the current-carrying part of the field, H_J, as the new flux emerges (see Figure 10). This flux is seemingly only a minor contributor to the overall active region during this time and close to potential as it does not significantly affect either the helicity content of the active region corona or the helicity of the current-carrying part of the field, H_J (Figure 10).

Phase 2 (February 13 00:00 to 07:00 UT), marks the time when the first significant rise in the helicity ratio is observed and when the ratio becomes greater than 0.1 (after ∼01:00 UT on February 13). We interpret, based on previous studies (Thalmann et al. 2019b; Moraitis et al. 2019; Gupta et al. 2021), that the coronal field may therefore be prone to an eruption during Phase 2. Although no white light was observed during this phase, an eruption occurred ∼02:10 UT February 13 (which is termed failed due to the observation of a CME in coronagraph data). From the computed parameters (Figure 10) we see that the flux emergence during this phase leads to a significant increase in the helicity of the current-carrying part of the coronal field, H_J, which then leads to a larger helicity ratio value. A reconfiguration of the coronal field in association with the failed eruption is associated with a broad peak in the helicity ratio of about 0.25 ∼04:00 UT February 13. A further episode of reconfiguration observed in the coronal field is evident by ∼05:30 UT February 13. Together, these activity events (although not ejective or associated with flaring activity) have a clear impact on the helicity content of the coronal field. Specifically, the events lead to a reduction in the helicity of the current-carrying field, H_J, and a levelling-off of the active region helicity content, H_V, and "potential" helicity of the volume-threading field, H_{PJ}. This is despite the still-increasing flux content of the region and indicates that the magnetic field has reconfigured to a more relaxed state. The helicity ratio then reduces accordingly (Figure 10). The evolution of the corona during this phase appears to be driven by the continued flux emergence and the formation of a new polarity inversion line in the center of the active region. This polarity inversion line has the negative field of Bipole 1 and Bipole 3 along its northern side and the positive field of Bipole 2 along the southern side. The formation of this polarity inversion line is analyzed in detail in Chintzoglou et al. (2019, in which the positive and negative polarities are termed P2 and N1 and the polarity inversion line the collisional polarity inversion line). The detailed study of Chintzoglou et al. (2019) shows the inversion line growing in length during Phase 2. During Phase 3 (February 13 07:00 to 19:00 UT), the helicity ratio begins to increase in magnitude again, but levels off briefly following the occurrence of a failed eruption. The helicity ratio remains at levels >0.25 throughout, indicating that the region could be prone to eruption. The ratio reaches a peak value of ∼0.45 around 17:00 UT, and only shows a notable decrease after the GOES M6.6-class flare and its associated CME. After this

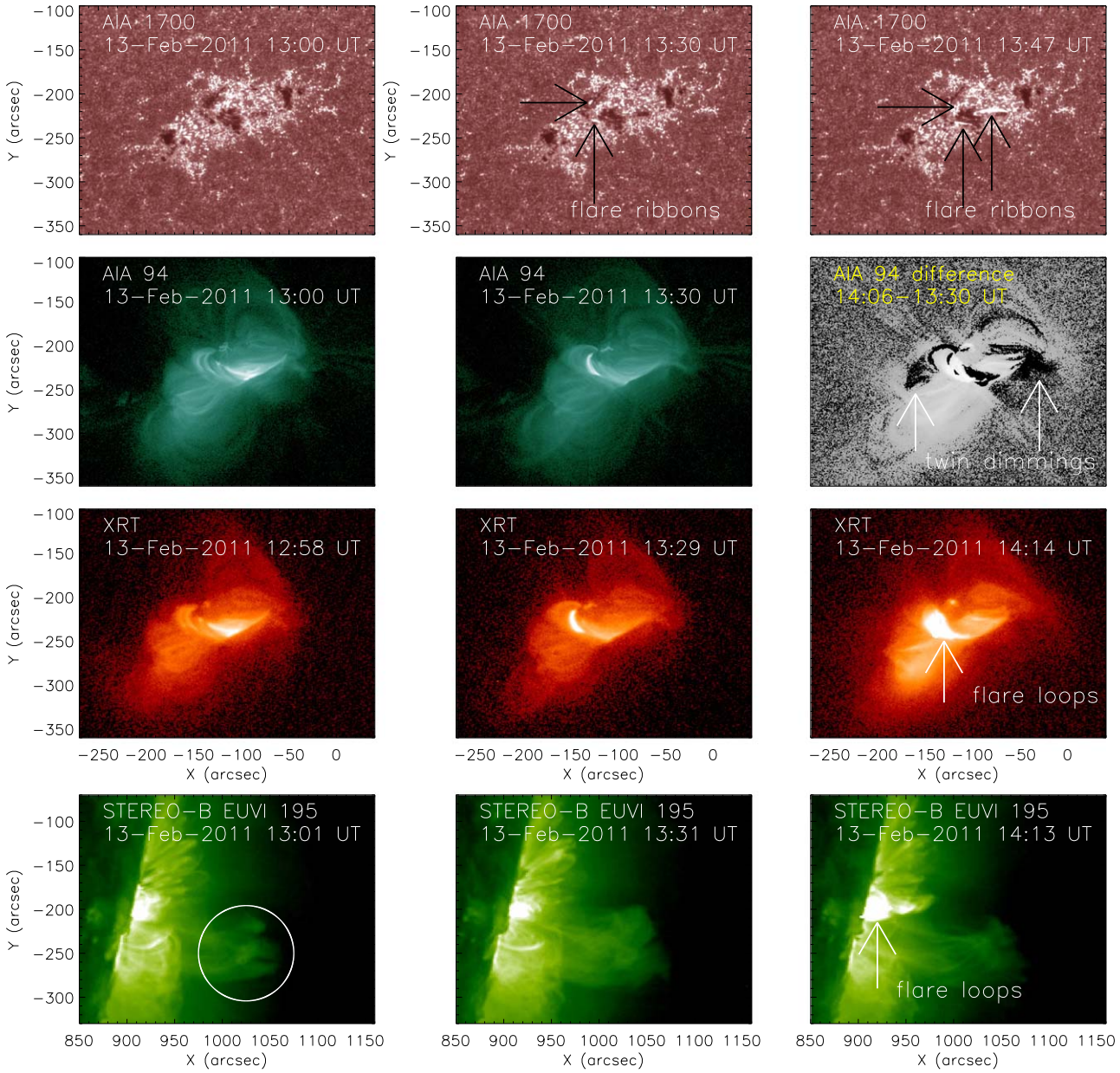

Figure 6. Phase 3 failed eruption: summary image showing the growth of EUV-emitting loops in NOAA active region 11158 followed by a failed eruption from the region during Phase 3. From top to bottom, the rows show data from AIA 1700 Å waveband, AIA 94 Å waveband data, XRT Ti Poly filter images, and STEREO-B EUVI 195 Å waveband data.

successful eruption the active region's helicity content (H_V) and the helicity of the current-carrying part of the field (H_J) both decrease in response to the ejection of current-carrying field, with the most significant change being that of the current-carrying part of the field. Hence, the ratio reduces accordingly (Figure 10). During Phase 3, the collisional polarity inversion line reaches an elongation that is maintained until Phase 5 (when a short-lived increase in length occurs; see Figure 7 in Chintzoglou et al. 2019). During Phase 4 (February 13 19:00 to February 14 12:00 UT), the helicity ratio reaches a peak value of 0.4 around 22:00 UT on February 13, in between the occurrence of jets. After this time, the helicity ratio value drops, temporally coincident with further (major) jet activity. There is no increase in the ratio in the time leading up to the CME that occurs 02:30 UT on February 14, although the helicity ratio remains at levels >0.25, indicating the potential for an eruption throughout this phase.

During Phase 5 (12:00 UT February 14 to 12:00 UT February 15) the helicity ratio shows variation, but of a much smaller magnitude than in the previous phases. However, it is during Phase 5 that the most energetic flare occurs. The helicity ratio increases from a value of 0.14 to a peak value of 0.22 prior to the GOES X2.2-class flare, then decreases from 0.16 to values below 0.1 around 12:00 UT (at the end of Phase 5). Although it may seem counterintuitive that the helicity ratio has lower values during the time period in which the most intense CME-related flaring occurs, it must be noted that the computed helicity ratio value is a product of an observational data set collected at a particular time, which may or may not fully capture the point just before the magnetic field configuration becomes unstable. Once the eruptions begin, no helicity ratio

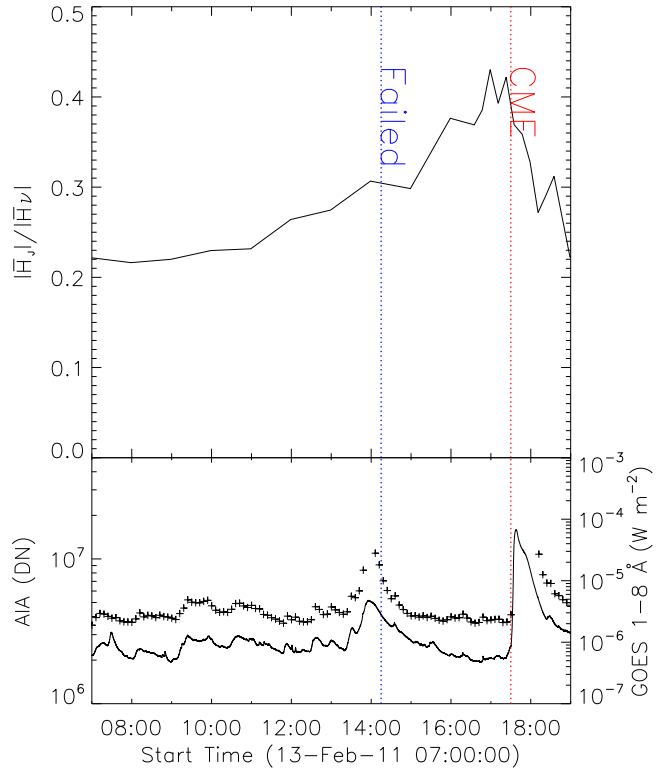

Figure 7. Evolution of the mean helicity ratio during Phase 3 (February 13 07:00 to 19:00 UT) is shown in the top panel (continuous line). The bottom panel shows the full Sun GOES 1–8 Å light curve (continuous line) and the AIA 131 Åactive region light curve. The vertical dotted blue (red) line indicates the time of a failed eruption (CME, i.e., successful eruption).

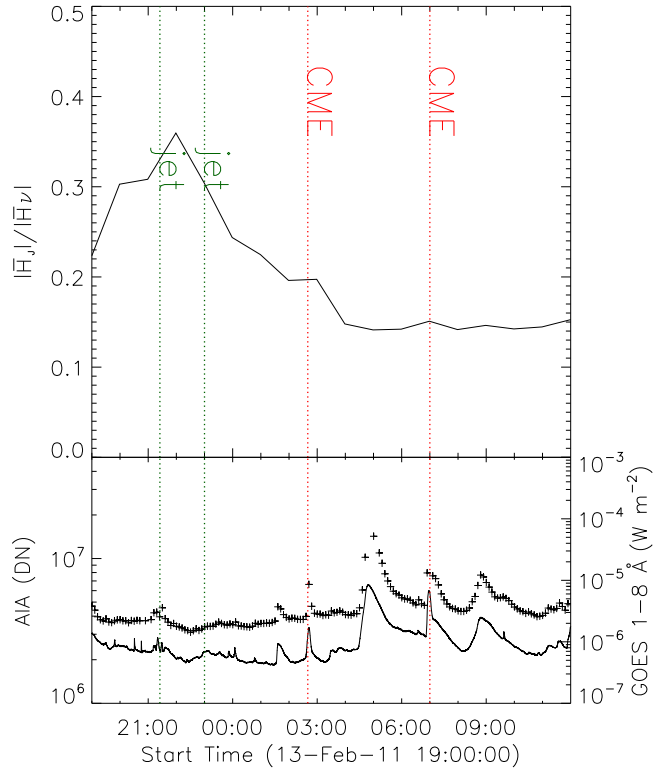

Figure 8. Evolution of the mean helicity ratio during Phase 4 (February 13 19:00 to February 14 04:00 UT) shown in the top panel (continuous line). The bottom panel shows the full Sun GOES 1–8 Å light curve (continuous line) and the AIA 131 Å active region light curve. The vertical dotted green (red) lines show the times of jets (CMEs).

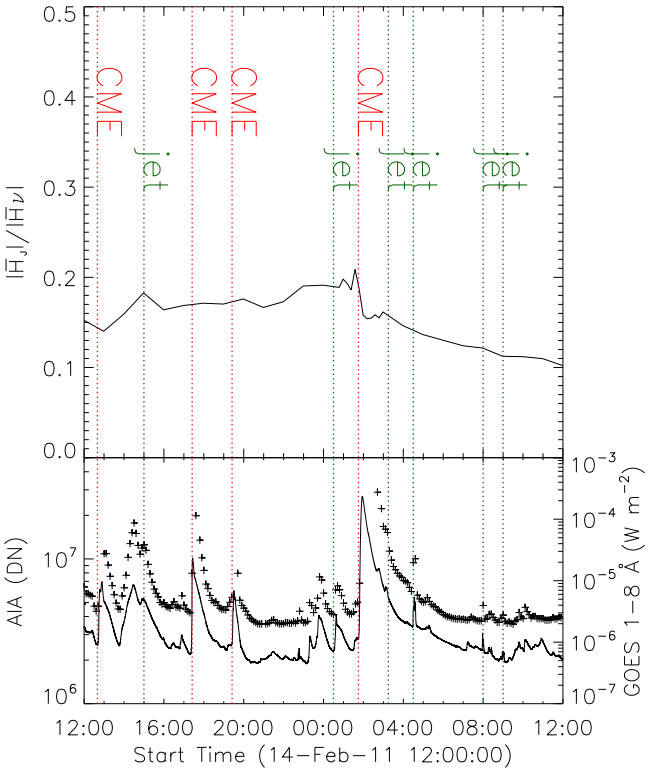

Figure 9. Evolution of the mean helicity ratio during Phase 5 (February 14 12:00 to 15 February 12:00 UT) is shown in the top panel (continuous line). The bottom panel shows the full Sun GOES 1–8 Å light curve (continuous line) and the AIA 131 Å active region light curve. The vertical dotted green (red) lines show the times of jets (CMEs).

can be computed from a NLFF model as by definition the system is unstable at that point. So, depending on the available data, one may observe a magnetic field configuration that is more or less close to instability, and therefore one may calculate a difference in helicity ratio value between different events.

Despite the seemingly more subtle variations in the helicity ratio, there are still important findings that can be drawn from the evolution of the computed parameters. The jet at 15:00 UT on February 14 is preceded by an increase in H_J and $|H_J|/|H_V|$. Prior to the X-class flare, there are a series of confined C-class flares in the active region and a jet (lower panel, Figure 9). During this time the helicity ratio remains approximately constant (as no successful eruption occurs), but the helicity of the current-carrying part of the field, H_J, shows an overall increase in magnitude but with some variation that includes a decrease during the confined flares and an increase after the jet, which is then rapidly followed by the X2.2-class flare and the CME. In association with the X2.2-class flare and CME the helicity, H_V, helicity of the current-carrying field, H_J, and "potential" helicity, H_{PJ}, all decrease, likely due to the ejection of current-carrying field and subsequent field relaxation. Following the X2.2-class flare and CME, the active region continues to be jet-productive during a time when the helicity ratio and the helicity of the current-carrying part of the field, H_J, are in decline. The helicity ratio reaches the threshold for eruption, 0.1, at the end of the phase and dips below this value at the end of Phase 5. The next eruption in the region does not occur until ∼14:20 UT on February 16, indicating that the eruptive potential dropped as the helicity ratio fell toward, and

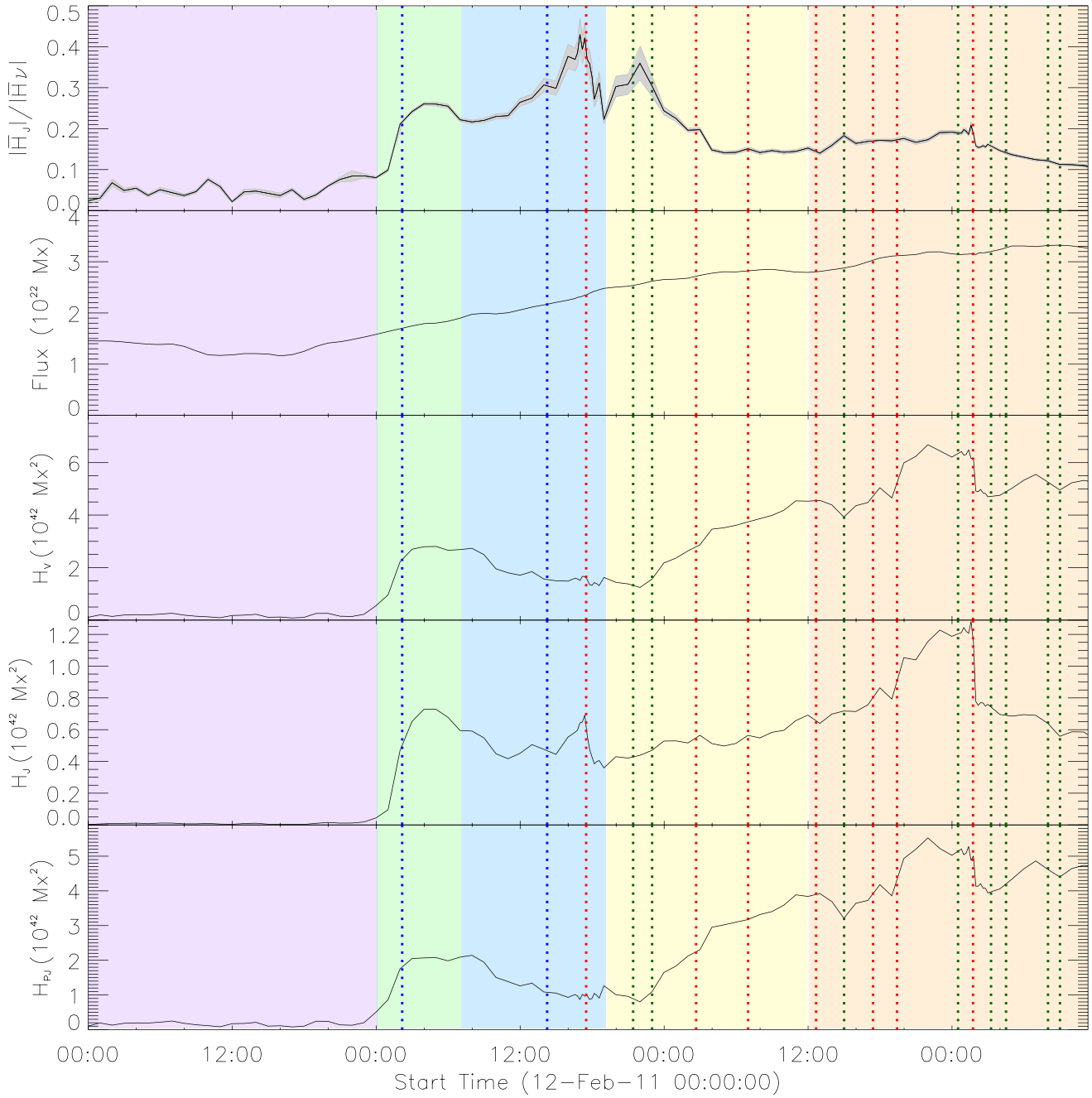

Figure 10. Summary figure showing the following computed parameters, from the top panel to the bottom: mean helicity ratio value as described in Section 1.4, with standard deviation indicated by the gray region, active region flux, mean relative helicity, mean helicity of the current-carrying flux, and the mean "potential" helicity of the volume-threading field. Vertical lines indicate the activity as shown in Figures 3 to 9 including failed eruptions (blue), successful eruptions (CMEs, red), and major jets (green). The five phases are also indicated in purple (Phase 1), green (Phase 2), blue (Phase 3), yellow (Phase 4), and orange (Phase 5).

then below, 0.1. It is noted that the helicity, H_V, and "potential" helicity, H_{PJ}, oscillate around the same value with perhaps an overall upward trend between the X2.2-class flare and the end of Phase 5.

The evolution of the helicity ratio, which has strong variations over time, can be contrasted with, for example, the evolution of energy and free energy content of the field. In the work of Sun et al. (2012), their Figure 4 shows how the unsigned flux, current, and free energy increase almost monotonically over time following the initial rise that begins late on 2011 February 12. In comparison, the helicity ratio evolution, and the components discussed here, reflect the evolving coronal configuration of the field, and may be a more suitable method to probe specific states that are prone to an eruption. In other words, free magnetic energy is a necessary but not sufficient condition for eruption. The helicity ratio in NOAA active region 11158 exceeds 0.1 between February 13 03:00 UT and February 13 12:00 UT, and it is during this time period that successful eruptions occur, supporting the findings of Gupta et al. (2021), which indicates a ratio above this value could be used in space weather forecasting.

The approach of analyzing the time evolution of the helicity ratio can also be compared with the approach of monitoring the total relative helicity content of an active region to probe its

likelihood for eruption. Some studies suggest that CMEs are the product of the accumulation magnetic helicity in a region over time (Rust 1994; Nindos & Andrews 2004; LaBonte et al. 2007; Tziotziou et al. 2012, 2013). Indeed, if only short timescales of a few hours are monitored, five out of the seven CMEs in this study are preceded by a rise in the relative magnetic helicity calculated for the active region. However, it has been shown that higher magnetic helicity content does not necessarily mean that a region is more likely to produce an eruption. Indeed, in the simulations of Pariat et al. (2017) the noneruptive magnetic field configurations possess a higher magnetic helicity content than do the eruptive configurations. It is also worth remembering that CMEs originate from a wide range of regions, from ephemeral regions with total magnetic flux content (ϕ) of $\sim 10^{20}$ Mx to large active regions with 10^{22} Mx, meaning that there will be no universal helicity threshold that must be reached before an eruption can occur (since magnetic helicity scales with ϕ^2).

Although this study focuses on the relationship between the helicity ratio evolution and eruptive activity from the corona, there are future opportunities to investigate the full range of drivers that evolve the coronal field and therefore may be mechanisms responsible for the helicity ratio changes. For example, detailed investigation not only of flux emergence but also photospheric flows that further evolve the magnetic field configuration, as detailed in Chintzoglou et al. (2019). NOAA active region 11158 did exhibit strong shearing motions of the photospheric magnetic field fragments as the magnetic field emerged, leading to reconnection between adjacent bipoles. This was particularly evident along the polarity inversion line that formed through the collision of opposite polarity field from bipoles 1, 2, 3, and 5. Magnetic connections formed across this inversion line as the flux emerged, and the photospheric flows meant that the newly connected field lines were subject to significant shearing motions during the entirety of February 13 (Chintzoglou et al. 2019). It is during this day (covering Phases 2 and 3 and the first part of Phase 4), when the coronal magnetic field is undergoing significant reconfiguration due to flux emergence, reconnection, shearing motions, and eruptions (failed and successful), that the helicity ratio shows the greatest variation. Rotation of some polarities was also observed, as detailed in Vemareddy et al. (2012). Their sunspot, labeled SN1, equates to the combined negative polarities of our Bipole 2 and Bipole 4. The authors find that SN1 has a high rotation in the counterclockwise direction during the time period ~04:00 to 22:00 UT on February 14. Their sunspot SP2 equates to the positive polarity of our Bipole 3 and Bipole 5, and they find the highest clockwise rotation of this spot to be between ~06:00 and 14:00 UT of February 14. This time period covers the second half of Phase 4 and the first part of Phase 5. This time period corresponds to a time when the flux emergence rate has reduced slightly and no major changes to the helicity ratio occur. The relative helicity of the magnetic field volume is increasing, however, implying that the magnetic field rotation is having an overall impact but with only a minor contribution to the helicity of the current-carrying part of the field. It is an open question as to whether the helicity ratio is more sensitive to helicity changes associated with flux emergence, i.e., influenced by the ϕ^2 scaling of helicity, than that caused by photospheric flows.

5. Conclusions

In this study, we relate the evolution of the helicity ratio, $|H_J|/|H_V|$ (helicity of the current-carrying part of the field to the total relative magnetic helicity within the volume), that was identified by Pariat et al. (2017) as a marker of eruptivity, in NOAA active region 11158 over a timescale of 4 days to observed activity including successful eruptions (CMEs), failed eruptions, and jets. The aim was to test the hypothesis that when a threshold of $|H_J|/|H_V| = 0.1$ is exceeded the active region enters a phase in which it is prone to eruption. We find that CMEs only occur in the active region in a time window during which the helicity ratio is above 0.1. When the ratio is less than 0.1, there are no successful eruptions. The helicity ratio as an indicator of eruption likelihood has already been tested in numerical simulations (Pariat et al. 2017) and in extrapolated fields (James et al. 2018; Thalmann et al. 2019b; Moraitis et al. 2019; Gupta et al. 2021), and this study builds on and supports these findings.

An advantage of the use of the helicity ratio to investigate active regions that are prone to an eruption is that the approach makes no assumption about the specific magnetic field configuration. Its novelty is that the time variation of the helicity ratio may indicate when key transitions occur in the coronal field in the run-up to an eruption, which might otherwise be overlooked.

NOAA active region 11158 was studied over 4 days, from 2011 February 12 to 2011 February 15, inclusive, and the timeline is split into five phases. During Phase 1, when the helicity ratio remains below the proposed threshold for eruption ($|H_J|/|H_V|<0.1$), we indeed observe no eruptive activity. The threshold is exceeded during Phase 2, which shows an increasing ratio value in the ~hour before a failed eruption. Likewise, in Phase 3, the threshold is exceeded and increases in the ratio are observed in the time leading up to both a failed and a successful eruption. During Phase 4, however, the major variations to the helicity ratio are temporally coincident with episodes of jet activity. This includes two episodes of jet occurrence, one before and one after, the peak in the helicity ratio. Although jets may be expected to have a more minor impact on the global properties of the active region, it is notable that small eruptions, through reconnection with surrounding large-scale fields, have been observed to lead to the redirection of plasma from the erupting structure along the larger-scale field to produce jets (see Figure 7; Green et al. 2017; Doyle et al. 2019). During Phase 4 the ratio remains above the threshold at all times, with a successful eruption taking place as the ratio is decreasing in value and later during a time of a small variation in the helicity ratio. During Phase 5, when the helicity ratio is still above the threshold level, the active region is a prolific producer of CMEs, major flares, and jets. The variations in the helicity ratio are more pronounced during Phases 2 and 3 and the first part of Phase 4, when the active region exhibits flux emergence, collision and reconnection between opposite polarity fields of different bipoles, strong shearing motion of the newly reconnected fields, and reconfiguration of the corona through failed and successful eruptions. During the later stages of Phase 4 and through Phase 5, when flux emergence and shearing motions have lessened, the signatures in the evolution of the helicity ratio are somewhat subtle. Thus, further dedicated studies are required to enable a more comprehensive understanding of the evolution

of the coronal magnetic field, the drivers of this evolution, and the subsequent impact on the helicity ratio.

L.M.G. is grateful to the Royal Society, that supported this research through the Royal Society University Research Fellowship scheme and NERC for funding via the SWIMMR Aviation Risk Modeling (SWARM) project (grant No. NE/V002651/1). J.T. acknowledges support from the Austrian Science Fund (FWF): grant No. P31413-N27. G.V. acknowledges support from the European Union's Horizon 2020 research and innovation program under grant agreement No. 824135, STFC grant No. ST/T000317/1, and funding by the Bundesministerium für Wirtschaft und Technologie through Deutsches Zentrum für Luft- und Raumfahrt e.V. (DLR) grant Nos. 50 OT 1001/1201/1901 as well as 50OT 0801/1003/1203/1703 and the President of the Max Planck Society (MPG). E.P. thanks the CNES and the Programme National Soleil Terre of the CNRS/INSU for financial support. L.L. highly appreciates and thanks the financial support from the European Union's Horizon 2020 research and innovation program under the grant agreement No. 870405. K.M. has received funding from the European Union's Horizon 2020 research and innovation program under the Marie Skłodowska-Curie grant agreement No. 893489. J.T., G.V., E.P., L.L. and K.M. benefited from discussions during the meetings of the ISSI International Team "Magnetic Helicity in Astrophysical Plasmas" (https://www.issibern.ch/teams/helicityastroplas/). SDO is a mission of NASA's Living With a Star Program. STEREO is the third mission in NASA's Solar Terrestrial Probes program. The authors thank the SDO and STEREO teams for making their data publicly accessible. The STEREO/SECCHI data used here are produced by an international consortium of the Naval Research Laboratory (USA), Lockheed Martin Solar and Astrophysics Laboratory (USA), NASA Goddard Space Flight Center (USA), Rutherford Appleton Laboratory (UK), University of Birmingham (UK), Max-Planck-Institut für Sonnensystemforschung (Germany), Centre Spatial de Liège (Belgium), Institut d'Optique Théorique et Appliqué (France), and Institut d'Astrophysique Spatiale (France). Hinode is a Japanese mission developed and launched by ISAS/JAXA, collaborating with NAOJ as a domestic partner, NASA and STFC (UK) as international partners. Scientific operation of the Hinode mission is conducted by the Hinode science team organized at ISAS/JAXA. This team mainly consists of scientists from institutes in the partner countries. Support for the post-launch operation is provided by JAXA and NAOJ (Japan), STFC (U.K.), NASA (U.S.A.), ESA, and NSC (Norway).

ORCID iDs

L. M. Green https://orcid.org/0000-0002-0053-4876
J. K. Thalmann https://orcid.org/0000-0001-8985-2549
G. Valori https://orcid.org/0000-0001-7809-0067
E. Pariat https://orcid.org/0000-0002-2900-0608
L. Linan https://orcid.org/0000-0002-4014-1815
K. Moraitis https://orcid.org/0000-0001-8900-5948

References

Antiochos, S. K., DeVore, C. R., & Klimchuk, J. A. 1999, ApJ, 510, 485
Berger, M. A. 1999, PPCF, 41, B167
Berger, M. A. 2003, in Advances in Nonlinear Dynamics, ed. A. Ferriz-Mas & M. Núñez (Boca Raton, FL: CRC Press), 345
Berger, M. A., & Field, G. B. 1984, JFM, 147, 133
Chen, P. F. 2011, LRSP, 8, 1
Chintzoglou, G., & Zhang, J. 2013, ApJL, 764, L3
Chintzoglou, G., Zhang, J., Cheung, M. C. M., & Kazachenko, M. 2019, ApJ, 871, 67
Dalmasse, K., Pariat, E., Valori, G., Démoulin, P., & Green, L. M. 2013, A&A, 555, L6
Démoulin, P. 2007, AdSpR, 39, 1674
Doyle, L., Wyper, P. F., Scullion, E., et al. 2019, ApJ, 887, 246
Finn, J. M., & Antonsen, T. M. 1985, PPCF, 9, 111
Forbes, T. G. 2000, JGR, 105, 23153
Forbes, T. G., & Isenberg, P. A. 1991, ApJ, 373, 294
Golub, L., Deluca, E., Austin, G., et al. 2007, SoPh, 243, 63
Green, L. M., Fuentes, M. C. L., Mandrini, C. H., Démoulin, P., & Driel-Gesztelyi, L. L. v. 2002, SoPh, 208, 43
Green, L. M., Török, T., Vršnak, B., Manchester, W., & Veronig, A. 2018, SSRv, 214, 46
Green, L. M., Valori, G., Zuccarello, F. P., et al. 2017, ApJ, 849, 40
Gupta, M., Thalmann, J. K., & Veronig, A. M. 2021, A&A, 653, 69
Howard, R. A., Moses, J. D., Vourlidas, A., et al. 2008, SSRv, 136, 67
James, A. W., Valori, G., Green, L. M., et al. 2018, ApJL, 855, L16
Jiang, Y., Zheng, R., Yang, J., et al. 2012, ApJ, 744, 50
Kliem, B., & Török, T. 2006, PhRvL, 96, 255002
Krausmann, E., Andersson, E., Gibbs, M., & Murtagh, W. 2017, Space weather & critical infrastructures: findings and outlook (Luxembourg: European Commission Publications Office))
LaBonte, B. J., Georgoulis, M. K., & Rust, D. M. 2007, ApJ, 671, 955
Lemen, J. R., Title, A. M., Akin, D. J., et al. 2012, SoPh, 275, 17
Linan, L., Pariat, E., Aulanier, G., Moraitis, K., & Valori, G. 2020, A&A, 636, A41
Linan, L., Pariat, É., Moraitis, K., Valori, G., & Leake, J. 2018, ApJ, 865, 52
Luoni, M. L., Francile, C., López, F. M., et al. 2017, BAAA, 59, 151
Moore, R. L., Sterling, A. C., Hudson, H. S., & Lemen, J. R. 2001, ApJ, 552, 833
Moraitis, K., Sun, X., Pariat, É., & Linan, L. 2019, A&A, 628, A50
Moraitis, K., Tziotziou, K., Georgoulis, M. K., & Archontis, V. 2014, SoPh, 289, 122
Nindos, A., & Andrews, M. D. 2004, ApJL, 616, L175
O'Kane, J., Green, L., Long, D. M., & Reid, H. 2019, ApJ, 882, 85
Pariat, E., Leake, J. E., Valori, G., et al. 2017, A&A, 601, A125
Patsourakos, S., & Georgoulis, M. K. 2017, SoPh, 292, 89
Price, D. J., Pomoell, J., Lumme, E., & Kilpua, E. K. J. 2019, A&A, 628, A114
Rust, D. M. 1994, GeoRL, 21, 241
Scherrer, P. H., Schou, J., Bush, R. I., et al. 2012, SoPh, 275, 207
Schmieder, B., Demoulin, P., Aulanier, G., & Golub, L. 1996, ApJ, 467, 881
Shibata, K., & Magara, T. 2011, LRSP, 8, 6
Sun, X., Hoeksema, J. T., Liu, Y., et al. 2012, ApJ, 748, 77
Temmer, M. 2021, LRSP, 18, 4
Thalmann, J. K., Linan, L., Pariat, E., & Valori, G. 2019a, ApJL, 880, L6
Thalmann, J. K., Moraitis, K., Linan, L., et al. 2019b, ApJ, 887, 64
Thalmann, J. K., Sun, X., Moraitis, K., & Gupta, M. 2020, A&A, 643, A153
Toriumi, S., Iida, Y., Bamba, Y., et al. 2013, ApJ, 773, 128
Toriumi, S., & Wang, H. 2019, LRSP, 16, 3
Tziotziou, K., Georgoulis, M. K., & Liu, Y. 2013, ApJ, 772, 115
Tziotziou, K., Georgoulis, M. K., & Raouafi, N.-E. 2012, ApJL, 759, L4
Valori, G., Pariat, E., Anfinogentov, S., et al. 2016, SSRv, 201, 147
van Ballegooijen, A. A., & Mackay, D. H. 2007, ApJ, 659, 1713
Vemareddy, P., Ambastha, A., & Maurya, R. A. 2012, ApJ, 761, 60
Wiegelmann, T., Petrie, G. J. D., & Riley, P. 2017, SSRv, 210, 249
Wiegelmann, T., & Sakurai, T. 2012, LRSP, 9, 5
Yeates, A. R., & Hornig, G. 2016, A&A, 594, A98
Zuccarello, F. P., Aulanier, G., & Gilchrist, S. A. 2015, ApJ, 814, 126
Zuccarello, F. P., Pariat, E., Valori, G., & Linan, L. 2018, ApJ, 863, 41